

An M-dwarf star in the transition disk of Herbig HD 142527

Physical parameters and orbital elements

S. Lacour^{1,2}, B. Biller³, A. Cheetham⁴, A. Greenbaum⁵, T. Pearce⁶, S. Marino⁶, P. Tuthill⁷, L. Pueyo⁸,
E. E. Mamajek⁹, J. H. Girard¹⁰, A. Sivaramakrishnan⁸, M. Bonnefoy¹¹, I. Baraffe^{9,12}, G. Chauvin¹¹,
J. Olofsson^{13,14,15}, A. Juhasz⁶, M. Benisty¹¹, J.-U. Pott¹³, A. Sicilia-Aguilar¹⁶, T. Henning¹³, A. Cardwell¹⁷,
S. Goodsell^{18,19}, J. R. Graham²⁰, P. Higon^{10,17}, P. Ingraham²¹, Q. Konopacky²², B. Macintosh²³, R. Oppenheimer²⁴,
M. Perrin⁸, F. Rantakyro¹⁷, N. Sadakuni²⁵, and S. Thomas²¹

(Affiliations can be found after the references)

Received 30 November 2015 / Accepted 25 April 2016

ABSTRACT

Aims. HD 42527A is one of the most studied Herbig Ae/Be stars with a transitional disk, as it has the largest imaged gap in any protoplanetary disk: the gas is cleared from 30 to 90 AU. The HD 142527 system is also unique in that it has a stellar companion with a small mass compared to the mass of the primary star. This factor of ≈ 20 in mass ratio between the two objects makes this binary system different from any other YSO. The HD 142527 system could therefore provide a valuable test bed for understanding the impact of a lower mass companion on disk structure. This low-mass stellar object may be responsible for both the gap and dust trapping observed by ALMA at longer distances.

Methods. We observed this system with the NACO and GPI instruments using the aperture masking technique. Aperture masking is ideal for providing high dynamic range even at very small angular separations. We present the spectral energy distribution (SED) for HD 142527A and B. Brightness of the companion is now known from the R band up to the M' band. We also followed the orbital motion of HD 142527B over a period of more than two years.

Results. The SED of the companion is compatible with a $T = 3000 \pm 100$ K object in addition to a 1700 K blackbody environment (likely a circum-secondary disk). From evolution models, we find that it is compatible with an object of mass $0.13 \pm 0.03 M_{\odot}$, radius $0.90 \pm 0.15 R_{\odot}$, and age $1.0_{-0.75}^{+1.0}$ Myr. This age is significantly younger than the age previously estimated for HD 142527A. Computations to constrain the orbital parameters found a semimajor axis of 140_{-70}^{+120} mas, an eccentricity of 0.5 ± 0.2 , an inclination of 125 ± 15 degrees, and a position angle of the right ascending node of -5 ± 40 degrees. Inclination and position angle of the ascending node are in agreement with an orbit coplanar with the inner disk, not coplanar with the outer disk. Despite its high eccentricity, it is unlikely that HD 142527B is responsible for truncating the inner edge of the outer disk.

Key words. protoplanetary disks – planet-disk interactions – binaries: visual – stars: variables: T Tauri, Herbig Ae/Be

1. Introduction

During the process of planet formation and disk dissipation, primordial disks begin in an optically thick state with significant emission at infrared wavelengths. As the disks clear out, they pass through an intermediate transitional stage marked by a drop in near- or mid-infrared (IR) emission that indicates the presence of an annular disk gap. These gaps can form through several mechanisms, such as photoevaporation, truncation due to a binary companion, or the presence of a forming planet. This last pathway has led to transitional disks being the subject of close study, as they may provide valuable insights into the planet formation process.

HD 142527A, a young stellar object (YSO), is one of the most studied Herbig Ae/Be stars with a transitional disk. With dust and some gases cleared from 30 to 90 AU, it has the largest imaged gap in any protoplanetary disk. According to Mendigutía et al. (2014), the age, distance, and mass for this star are 5 ± 1.5 Myr, 140 ± 20 pc and $2.0 \pm 0.3 M_{\odot}$, respectively. Biller et al. (2012) discovered a low-mass stellar companion ($\sim 0.2 M_{\odot}$) at ≈ 12 AU from the star within the gap. This companion was confirmed in the R band by Close et al. (2014). Eccentric orbit or not, it may have played a vital role in carving the large gap in this system.

HD 142527A is also notable for its diversity of disk structure. Recent imaging with the Atacama Large Millimeter Array (ALMA) of the outer disk (Casassus et al. 2013, 2015b) reveals large asymmetrical structures composed of millimeter-size grains (similar to the rare horseshoe structure also seen around the young Herbig star WLY 2-48 by van der Marel et al. 2013). These structures are thought to be signposts of density variations possibly caused by planetary formation (Williams & Cieza 2011). Scattering of the stellar light in the near-infrared (NIR) also reveals structures at the surface of the outer disk (Avenhaus et al. 2014).

The HD 142527 system provides a valuable test bed for understanding the impact of a lower mass companion on disk structure. As opposed to other young stellar binaries, which generally have nearly equal masses, the HD 142527 system has a more extreme mass ratio (a factor of ~ 20). Thus, we can study in situ the effects of this companion, which may be responsible for both the gap and dust trapping observed further out in this disk. However, initial constraints on the mass and other properties of the companion are still vague and at its present apparent separation it does not appear to be responsible for clearing the large disk gap. Many studies have invoked the possibility of forming giant planets on wide orbits exterior to the companion, making HD 142527

an exciting target for direct imaging observations. Constraining the mass and orbital parameters of the low-mass companion is vital to determining the origin of the observed disk gap.

We have been conducting ongoing orbital monitoring to constrain the companion properties. This paper reports multiple aperture masking observations of HD142527B. The interferometric nature of the technique permits precise measurements of the contrast ratio and separation, even though the companion lies at the diffraction limit of the telescope. In Sect. 2, we present the new sparse aperture masking (SAM) observations. In Sect. 3, we review the basic parameters of HD 142527A. In Sect. 4, we report and discuss the spectral energy distribution (SED) of the companion from visible to mid-infrared ($5\ \mu\text{m}$) light. In Sect. 5, we present the orbital parameters of the companion. In Sect. 6, we discuss the results.

2. Observations and data reduction

2.1. Principle

Nonredundant aperture masking (NRM), also called SAM allows a single aperture telescope to be used as a Fizeau interferometer. This is accomplished by dividing the aperture of the telescope into multiple subapertures using a mask in the pupil plane of the telescope, then allowing light from the subapertures to interfere. The point spread function (PSF) is thus transformed into a pattern made of multiple fringes. Measuring the amplitude and phase of these fringes allows us to retrieve information to the diffraction limit of the telescope and beyond. The use of closure phases with SAM also enables high contrast capability, as closure phases are an estimator robust to atmospheric and optical aberrations (Knox 1976).

2.2. Datasets and image reconstruction

We observed HD 142527 with two instruments: NACO at the VLT, and the Gemini Planet Imager (GPI) on the Gemini South telescope. Both instruments are equipped with NRM masks. We used a 7-hole on NACO (Tuthill et al. 2010) and the 10-hole on GPI (Greenbaum et al. 2014).

New NACO data were obtained in March 2013 and July 2013. All NACO data were reduced with the SAMP pipeline (Lacour et al. 2011). The two calibrators HD 142695 and HD 144350 were interleaved with the observations. We reanalyzed the March 2012 NACO data from Biller et al. (2012) to remove HD 142384 as a calibrator, which turned out to be a close binary system (Le Bouquin 2014). The new reduction also benefits from recent updates to the SAMP pipeline to include a post-processing atmospheric dispersion corrector.

The GPI data were obtained in May 2014 in the J band. Calibrator HD 142695 was observed immediately afterward to remove instrumental effects. The GPI data reduction pipeline (Perrin et al. 2014, and references therein) was used to extract images in 37 wavelength channels, of which 17 are expected to be independent. Measured uncertainties were scaled to take this effect into account. The GPI pipeline corrects for flexure, bad pixels, and distortion in the two-dimensional (2D) frame. Argon lamp arcs taken right before the observations were used to calibrate wavelength and correct for shifts in position of microspectra due to flexure (Wolf et al. 2014). The data were dark subtracted and assembled into data cubes. The data cubes were then processed using the aperture masking pipeline developed at Sydney University with the closure phases and visibilities measured in different wavelength channels treated independently.

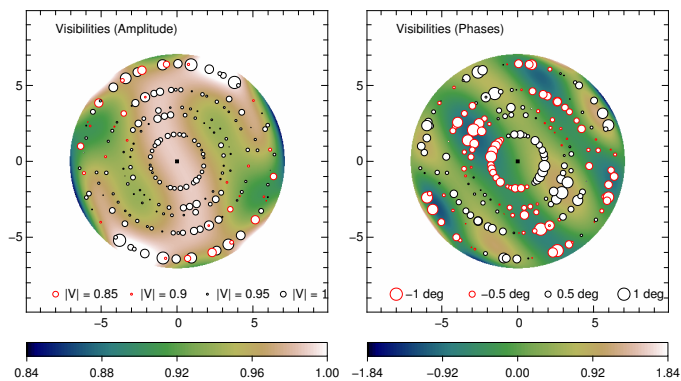


Fig. 1. SAM K band dataset. The phase and amplitude in the Fourier domain are represented by the size and color of the open circles. The units are normalized visibility for the amplitudes (*left panel*) and degrees for the phases (*right panel*). The color continuum below the data point are obtained by fitting Zernike polynomials to the data. The diagonal stripes observed on the phases are typical of a binary system.

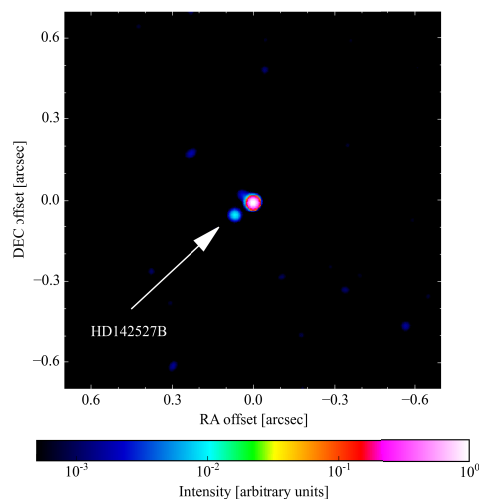


Fig. 2. SAM K band image reconstruction generated using the MIRA reconstruction software (Thiébaut 2008).

These data were fit with a three-parameter binary model (separation, position angle, and contrast ratio), with the contrast ratio assumed to be constant across the wavelength channels.

To illustrate the typical data produced by NRM, the K s band data obtained in July 2013 are presented in Fig. 1. The u - v frequency domain is limited by the diameter of the 8-m telescope. The amplitudes (visibilities) are normalized by the contrast observed on the calibrators. The right panel shows the phase derived from the closure phase. The closure phase to phase relation was established by singular value decomposition of the closure phase-to-phase matrix. Missing phase parameters (piston, tip, tilt, etc...) are set to zero.

We used closure phases and amplitudes to reconstruct a high resolution deconvolved image with the MIRA software (Thiébaut 2008). The resulting high resolution deconvolved image is shown for the July 2013 K s band dataset in Fig. 2. We performed the image synthesis using a nonparametric least-squares modeling technique over the amplitudes and closure phases, and adding a regularization term called “ x smooth” ($\ell_2 - \ell_1$ smoothness constraint). A point-source model image was used as seed for the image reconstruction. We found that the companion detection is robust to different regularization methods.

Table 1. Observations and contrast ratio.

Instrument	Spectral band	Date	Δmag
MagAO ⁽¹⁾	H α cont	11 April 2013	7.5 ± 0.25
GPI ⁽²⁾ (Imaging)	<i>Y</i> band	25 April 2014	3.2 ± 0.5
NACO (SAM)	<i>J</i> band	17 March 2013	5.0 ± 0.6
		14 July 2013	5.0 ± 0.2
GPI (SAM)		12 May 2014	4.63 ± 0.04
NACO (SAM)	<i>H</i> band	11 March 2012	4.5 ± 0.5
NACO (SAM)	<i>Ks</i> band	11 March 2012	4.80 ± 0.09
		17 March 2013	4.78 ± 0.07
		14 July 2013	4.67 ± 0.05
NACO (SAM)	<i>L'</i> band	11 March 2012	5.16 ± 0.11
		17 March 2013	5.36 ± 0.09
NACO (SAM)	<i>M'</i> band	17 March 2013	5.77 ± 0.34
		14 July 2013	5.80 ± 0.16

References. (1) [Close et al. \(2014\)](#); (2) [Rodigas et al. \(2014\)](#).

2.3. Companion fitting

Parameters describing the companion were extracted through model fitting to the closure phase data only, discarding the visibilities. At each epoch of observation, a single position was simultaneously fitted to all spectral bands to better constrain the flux ratio at long wavelengths. The model fitted to the closure phase is the following:

$$CP(\mathbf{u}, \mathbf{v}, \lambda) = \arg [1 + \rho_\lambda \exp(2i\pi(\boldsymbol{\alpha} \cdot \mathbf{u})/\lambda)] \\ + \arg [1 + \rho_\lambda \exp(2i\pi(\boldsymbol{\alpha} \cdot \mathbf{v})/\lambda)] \\ + \arg [1 + \rho_\lambda \exp(-2i\pi\boldsymbol{\alpha} \cdot (\mathbf{u} + \mathbf{v})/\lambda)], \quad (1)$$

where λ is the wavelength, and (\mathbf{u}, \mathbf{v}) the two baseline-vectors that compose the closure phase triangle. The free parameters of the fit are: i) the separation vector $\boldsymbol{\alpha}$ and ii) ρ_λ , the flux of the secondary with respect to the primary. The separation $\boldsymbol{\alpha}$ is wavelength independent, but the flux of the secondary depends on the filter bandpass (from *J* band to *M'* band). This procedure helps mitigate the problem of limited angular resolution at longer wavelengths.

The best solution for $\boldsymbol{\alpha}$ is achieved by taking the minimum value of the 2D χ^2 map. The map is obtained by regression over the free parameters ρ_λ . The map is then normalized to a reduced χ^2 of one, and the three sigma errors are determined from the area below which the reduced χ^2 is less than 10. An example of such a map is given in the central panel of Fig. 1 in [Billier et al. \(2012\)](#).

Finally, we determined the flux ratio for each filter, ρ_λ , adopting the position (including its error) obtained at each epoch. The flux ratios between the central star (including the unresolved part of the inner disk) and the companion are presented in Table 1. Unless stated otherwise, errors mentioned in this paper are 1 sigma.

3. HD 142527A

3.1. Distance, age, and mass

We adopt a distance of 140 ± 20 pc based on the arguments made by [Mendigutía et al. \(2014\)](#), namely that the star is near the Lupus IV cloud, and shares the proper motion and radial velocity of neighboring Sco-Cen stars (e.g., [Preibisch & Mamajek 2008](#)). The proper motion of the star ($\mu_\alpha = -17.2$ mas/yr, $\mu_\delta = -18.0$ mas/yr; [van Leeuwen 2007](#)) is similar to that of

overall proper motion of stars associated with the Lupus clouds ($\mu_\alpha = -16.0$ mas/yr, $\mu_\delta = -21.7$ mas/yr; [Galli et al. 2013](#)). The star is likely to be co-distant with either the Lupus clouds ([Galli et al. 2013](#)) or Upper Cen-Lup subgroup of Sco-Cen (~ 142 pc de Zeeuw et al. 1999), which surrounds the Lupus clouds.

[Mendigutía et al. \(2014\)](#) used an X-Shooter spectrum to constrain the temperature and the [Yi et al. \(2001\)](#) tracks to estimate the age and mass of HD 142527A. These do provide a dense grid of tracks for masses of $\sim 2 M_\odot$. However evolution models can be prone to systematic error in age and mass, especially for young stars. Therefore, we run the star parameters through different isochrone pre-main-sequence track models. When we adopt the $T_{\text{eff}} = 6550 \pm 100$ K and luminosity $L = 16.3 \pm 4.5 L_\odot$ from [Mendigutía et al. \(2014\)](#), we get the following age and mass pairs:

[D'Antona & Mazzitelli \(1997\)](#) tracks:

- $\log(\text{age/yr}) = 6.69 + 0.07 - 0.15(1\sigma) + 0.13 - 0.39(2\sigma)$
- $\text{age}(\text{Myr}) = 4.9 + 0.8 - 1.4(1\sigma) + 1.8 - 2.9(2\sigma)$
- $\text{Mass}(M_\odot) = 2.08 + 0.24 - 0.13(1\sigma) + 0.72 - 0.25(2\sigma)$

[Siess et al. \(2000\)](#) tracks:

- $\log(\text{age/yr}) = 6.80 + 0.11 - 0.12(1\sigma) + 0.21 - 0.25(2\sigma)$
- $\text{age}(\text{Myr}) = 6.3 + 1.7 - 1.5(1\sigma) + 3.9 - 2.7(2\sigma)$
- $\text{Mass}(M_\odot) = 2.01 + 0.21 - 0.18(1\sigma) + 0.48 - 0.33(2\sigma)$

[Yonsei-Yale \(Yi et al. 2003\)](#) tracks:

- $\log(\text{age/yr}) = 6.70 + 0.11 - 0.13(1\sigma) + 0.24 - 0.27(2\sigma)$
- $\text{age}(\text{Myr}) = 5.0 + 1.5 - 1.3(1\sigma) + 3.7 - 2.3(2\sigma)$
- $\text{Mass}(M_\odot) = 2.07 + 0.21 - 0.18(2\sigma) + 0.46 - 0.37(2\sigma)$.

We adopt a mass of $2.05 M_\odot$, with a statistical and observational error of $\pm 0.2 M_\odot$. We add a systematic error of $\pm 0.04 M_\odot$ from the tracks, assuming these three sets of tracks are sampling our ignorance in composition in physics. However, we conclude that the values given by [Mendigutía et al. \(2014\)](#) are a good approximation: a mass of $2.0 \pm 0.3 M_\odot$ and an age of 5.0 ± 1.5 Myr.

3.2. Spectral energy distribution

We plot the SED for HD 142527A in Fig. 3. We computed the SED from the fluxes reported by [Verhoeff et al. \(2011\)](#), as compiled in Table 2. Dust reddening was obtained from dust models by [Weingartner & Draine \(2001\)](#) ($R_V = 3.1$). Following [Verhoeff et al. \(2011\)](#), we used a visible extinction $A_V = 0.6$ mag, which includes the extinction by the interstellar medium and by the circumstellar material. This is in rough agreement with the excess color estimated by [Malfait et al. \(1998\)](#) and [Mendigutía et al. \(2014\)](#) of $E(B - V) = 0.33$ and 0.25 mag, respectively.

We obtain the blue spectral curve presented in Fig. 3 by adjusting a synthetic model of stellar atmosphere to the HD 142527A dereddened fluxes. We used a [Allard et al. \(2012\)](#) DUSTY model of temperature 6500 K and density $\log(g) = 4.0$. The main objective was to determine the *R* band continuum emission of HD 142527A. The result is within the error bar of using a temperature model of 6550 K and $\log(g)$ of 3.75 as derived by [Mendigutía et al. \(2014\)](#). The *R* band continuum flux is reported in Table 2.

4. Physical parameters of HD 142527B

4.1. Spectral energy distribution

We fit the SED of HD 142527B with a combination of stellar emission and dust emission from the circumsecondary disk. The

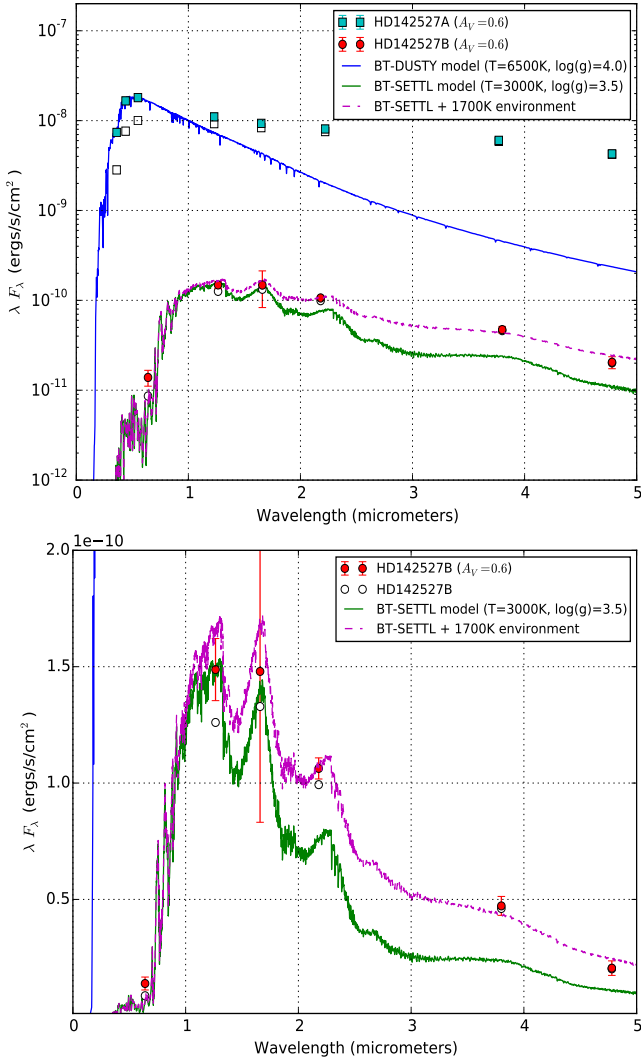


Fig. 3. Spectral energy distribution of HD 142527 A and B. The empty symbols are uncorrected for reddening. The filled symbols include correction for a dust opacity of visible absorption magnitude $A_V = 0.6$. Blue and green curves are stellar models of both stars from Allard et al. (2012).

dust emission is approximated by a blackbody of temperature 1700 K, which is close to the sublimation limit of dust particles. We used the BT-SETTL models computed by Allard et al. (2012)¹ to fit the stellar component of the SED. The parameters of this model are a temperature of 3000 K and a surface gravity of $\log(g) = 3.5$.

We find that the dust component modeled as a 1700 K blackbody emission primarily fits the longer wavelengths in the SED, while the J and R band emission is emitted almost exclusively (>90%) from the stellar surface. Thus, we can derive the temperature of the stellar surface from the $J - R$ color of the object.

The absolute magnitudes are reported in the right column of Table 2. These values are computed using a distance of 140 pc and dereddened using the algorithm determined by (Cardelli et al. 1989). In the following study, we adopt a J band absolute magnitude of 5.23 ± 0.1 mag. The absolute magnitude includes an additional 0.1 mag, corresponding to $\approx 10\%$, to remove circumstellar emission. Dust emission is assumed to be negligible in the R band.

¹ <http://perso.ens-lyon.fr/france.allard/>

Table 2. Visible and near-infrared fluxes of HD 142527B.

Band	Δmag	HD 142527A [Jy]	HD 142527B [mJy]	HD 142527B [Abs. Mag.]
R_{cont}	$7.5 \pm 0.25^{(1)}$	$1.8 \pm 0.2^{(3)}$	1.8 ± 0.3	9.3 ± 0.3
J	4.63 ± 0.04	$3.8 \pm 0.1^{(2)}$	53 ± 2	5.13 ± 0.05
H	4.5 ± 0.5	$4.6 \pm 0.1^{(2)}$	74 ± 32	4.6 ± 0.5
K_S	4.72 ± 0.04	$5.6 \pm 0.1^{(2)}$	72 ± 3	4.1 ± 0.1
L'	5.26 ± 0.08	$7.4 \pm 0.3^{(2)}$	58 ± 5	3.4 ± 0.1
M'	5.79 ± 0.16	$6.7 \pm 0.3^{(2)}$	32 ± 5	3.5 ± 0.2

Notes. Absolute magnitudes are obtained assuming a distance of 140 pc and dereddened from an $A_V = 0.6$ dust absorption.

References. (1) Close et al. (2014); (2) Verhoeff et al. (2011); (3) from SED using Castelli & Kurucz (2004) stellar models.

Hence, we obtain $(R - J)_{\text{HD 142527B}} = 4.17 \pm 0.3$ mag, where the error is dominated by the R band contrast ratio uncertainties. According to the catalog of stellar surface colors from Allard et al. (2012), we derive an effective temperature of $T_{\text{HD 142527B}} = 3000 \pm 100$ K, assuming $\log(g) = 3.5$.

4.2. Estimation of mass, age, and radius

The ratio between the radius of HD 142527A and HD 142527B can be estimated from the relative magnitude and effective temperatures of the stars. It is $R_{\text{HD 142527A}}/R_{\text{HD 142527B}} = 2.8 \pm 0.2$ if we assume an effective temperature of 6500 K for the primary and 3000 K for the secondary.

The mass, age, and absolute radius can be obtained from the absolute magnitudes, however, it requires prior knowledge of the evolution process of the star. Thus, we used the standard evolutionary model from Baraffe et al. (2015). This model does not assume any accretion during the evolution of the system. We plotted in Fig. 4 the isochrone and isomass of the star as a function of the temperature and R and J absolute magnitudes. According to these models, a suitable set of parameters are $M_{\text{HD 142527B}} = 0.13 \pm 0.03 M_{\odot}$, $R_{\text{HD 142527B}} = 0.90 \pm 0.15 R_{\odot}$ and an age of $1.0_{-0.75}^{+1.0}$ Myr. All errors are 1 sigma.

5. Orbital elements of HD 142527B

5.1. Small arc analysis

Known separations and position angles of HD 142527B with respect to HD 142527A are presented in Table 3. This includes all SAM observations, plus two MagAO observations (Close et al. 2014; Rodigas et al. 2014) and one GPI polarimetric observation (Rodigas et al. 2014). We included the two MagAO observations in our analysis, but did not include the GPI polarimetric observation (obtained through direct imaging). This GPI observation is far off the other measurements, possibly because of scattered emissions that biased the determination of the barycenter.

This dataset covers two years of observations, but only a small arc of the orbit is observed, corresponding to 15 degrees in position angle. The first approximation is therefore to consider that our knowledge is limited to a position and a velocity vector, projected on the plane of the sky. Thus, the position and velocity orthogonal to the plane of the sky remain unknown and prevent us from fully characterizing this orbit. However, we can still place constraints on some of the orbital parameters. From our data listed in Table 3, we computed a vector position $(x, y) = (68.0 \pm 0.7, -47)$ mas and a vector speed

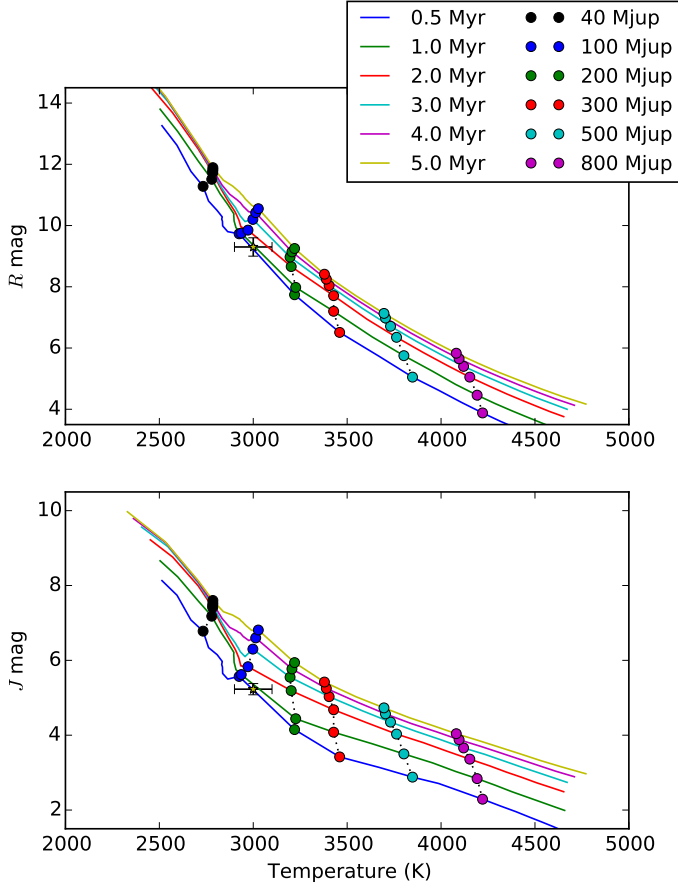


Fig. 4. Isocontours of masses and ages as a function of temperature and absolute magnitude, according to evolutionary models from Baraffe et al. (2015). The central asterisk correspond to HD 142527B. HD 14252A, with an effective temperature of the order of 6500 K, lies outside the plot and outside the temperature range of the model.

$(\dot{x}, \dot{y}) = (2.0 \pm 0.9, 13.4 \pm 0.9)$ mas/yr. The position in right ascension is labeled x and y for the declination. The y value was arbitrarily fixed to -47 mas to force the determination of the true anomaly at this declination (the choice of this fixed parameter does not affect the orbital elements). Finally, we defined μ as a scaled mass parameter that characterizes the acceleration at any given angular separation,

$$\mu = GM/d^3 = 4\pi^2 \left(\frac{M}{M_\odot} \right) \left(\frac{d}{\text{pc}} \right)^{-3} \text{ arcsec}^3/\text{year}^2, \quad (2)$$

where G is the gravitational constant. We used $M = 2.2 M_\odot$ as the total mass of the binary system and $d = 140$ pc for the distance of the binary system. Hence, for the HD 142527AB system

$$\mu = 3.2 \times 10^{-5} \text{ arcsec}^3/\text{year}^2. \quad (3)$$

The assumption that the companion is gravitationally bound to the main stellar object (eccentricity below or equal to 1) allows us to delimit a parameter space for the z and \dot{z} components. This (z, \dot{z}) parameter space is illustrated in Fig. 5 with dashed lines. The contours represent the six different parameters of the orbit. They correspond to the semimajor axis a in mas, the eccentricity e , the inclination i relative to the sky plane, the position angle of the ascending node, the argument of the periastris, and the true anomaly at which the companion reaches $y = -47$ mas. All

Table 3. HD 142527 B orbital observations.

Instrument	Date	Sep (mas)	PA (deg)
NACO (SAM)	11 March 2012	89.7 ± 2.6	133.1 ± 1.9
NACO (SAM)	17 March 2013	82.0 ± 2.1	126.3 ± 1.6
MagAO ⁽¹⁾	11 April 2013	86.3 ± 1.9	126.6 ± 1.4
NACO (SAM)	14 July 2013	82.5 ± 1.1	123.8 ± 1.2
MagAO ⁽²⁾	April 2014	79.7 ± 5.6	119.5 ± 8.7
GPI (Direct) ⁽²⁾	25 April 2014	88.2 ± 10.1	123.0 ± 9.2
GPI (NRM)	12 May 2014	77.2 ± 0.6	116.6 ± 0.5

References. (1) Close et al. (2014); (2) Rodigas et al. (2014).

elements are derived following the methodology described by Pearce et al. (2015).

Without any prior knowledge or probabilistic knowledge on z and \dot{z} , Fig. 5 can be interpreted that any semimajor axis, eccentricity, or inclination within the dashed contours is possible. For example, the semimajor axis can go from 52 mas to infinity.

5.2. Full determination of the orbital parameters

We also investigate possible orbits using a Markov chain Monte Carlo (MCMC) analysis as an alternative to the small arc technique presented in the previous section. Such an alternative technique has already been used for small arc dataset (e.g., on Fomalhaut by Kalas et al. 2013). This method also has the advantage to better benefit from individual observational errors over multiple observations.

We used the MCMC python library emcee (Foreman-Mackey et al. 2013). We computed the walkers for the variables $(x, z, \dot{x}, \dot{y}, \dot{z})$ and converted them to a probability distribution function for the orbital parameters. Any corresponding orbital element with an eccentricity above 1 was given a probability of zero. Within this boundary condition, the z and \dot{z} are given uniform prior distributions. The position angle of the ascending node was forced to lie between -90 and 90 degrees. The relation between $(x, y, z, \dot{x}, \dot{y}, \dot{z})$ and the orbital parameters are given in Appendix B of Pearce et al. (2015).

The results from the MCMC simulation are presented in Fig. 7. Unfortunately, the small range of position angles covered by our dataset does not strongly constrain the orbital elements. Within 1 sigma probability (68% of the results), they are the following: a semimajor axis $a = 140^{+120}_{-70}$ mas, an eccentricity $e = 0.5 \pm 0.2$, an inclination of $i = 125 \pm 15$ degrees, and an angular position of the right ascending node of -5 ± 40 degrees.

The angle of the periastron is the least constrained parameter. Two distinct families of orbits emerged from this simulation: one with a periastron around 40 degrees and the other at a periastron around 200 degrees. These two families of orbits are presented in Fig. 6. In this figure, all the gray curves have equal probabilities. The blue and red curves correspond to a maximum of probability. The first family, shown with the blue curve, corresponds to a trajectory where the companion has just passed the periastron. The second family, shown with the red curve, corresponds to a trajectory where the companion is going to pass the periastron.

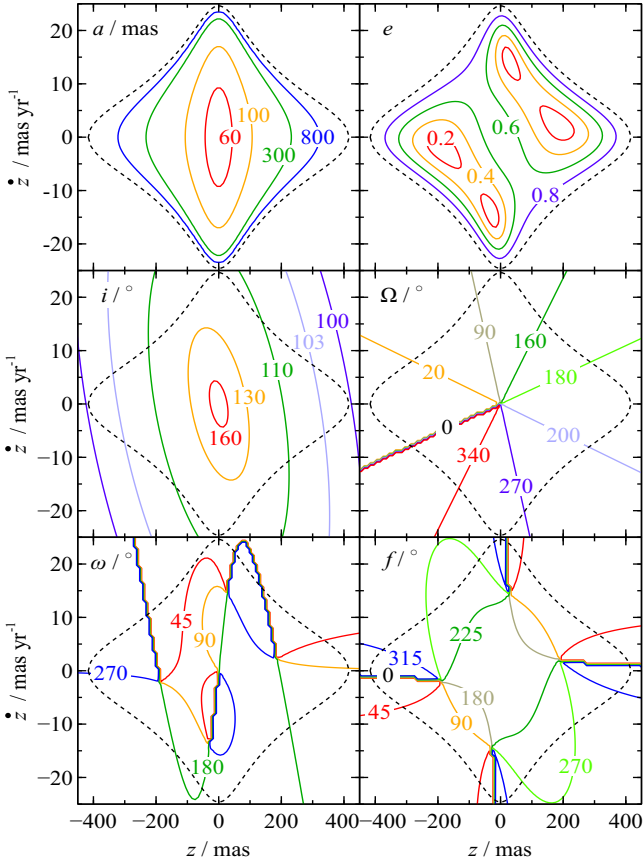


Fig. 5. Orbital elements of the system for different z and \dot{z} values. The contours are obtained by assuming a total system mass of $M_{\text{AB}} = 2.2 M_{\odot}$ and a distance to the system of $d = 140$ pc.

6. Discussion

6.1. Summary

Biller et al. (2012) observed a NIR excess around HD 142527B. Without a proper estimation of the level of NIR emission from the circumsecondary disk, it was difficult to be conclusive about the mass. In this work, we extended our observational baseline to the M band, but more importantly to the J band. We were able to model the NIR emission and conclude that the J band was mostly unaffected by the circumsecondary emission (to the 10% level).

If we assume that the NIR emission is caused by a circumsecondary environment, we can focus on the shorter wavelength observations (R and J band observations) to determine the parameters of the star. The result is that HD 142527B is a fairly standard young low-mass star that matches standard evolution mechanisms. However, at least according to the Baraffe et al. (2015) models, this last statement is only valid if we assume an age of $1.0^{+1.0}_{-0.75}$ Myr.

6.2. Age of the system

If we increase the age of the system to 5 Myr (according to Mendigutía et al. 2014), then the colors of the companion start to disagree with its absolute magnitudes. To reconcile a more advanced age with our observations, we would have to increase the apparent magnitude (make the star fainter). For the magnitudes to agree in the HR diagrams of Fig. 4 with an age of 5 ± 1.5 Myr,

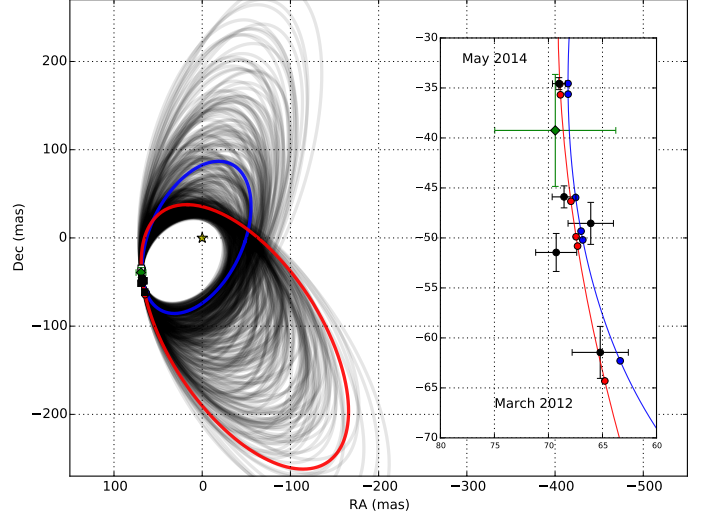


Fig. 6. Likely orbits for HD 142527B from MCMC simulation. The red and blue curves correspond to maximum likelihood parameters. The gray curves indicate possible solutions from the MCMC computations. The SAM observations indicate black squares. The green lozenge corresponds to a MagAO observation reported by Rodigas et al. (2014).

we would have to add 1.0 and 1.5 mag to the R and J band magnitudes, respectively. That would put the target at 70 pc, which is not compatible with the distance estimated in Sect. 3.1. Dust absorption would only decrease the absolute magnitude, giving an opposite effect.

Although previous episodes of intense accretion can change the structure and thus the position of a young object in a magnitude-temperature diagram, it seems difficult to invoke accretion effects to get an age of 5 Myr, instead of 1 Myr, for the observed luminosity of the low-mass companion. As discussed in Baraffe et al. (2009, 2012), cold accretion would have the opposite effect. The only, very unlikely possibility, would be for the low-mass star to have had a previous episode of intense hot accretion that would increase its luminosity and radius. The object would thus look younger than its nonaccreting counterpart. This accretion episode, however, should be recent. Otherwise, the object would have time to contract back to a size compatible with the models.

The age estimations of HD 142527 A and B rely on evolutionary models that have their own intrinsic source of errors. It has been shown that these uncertainties can be well above a few million years (Soderblom et al. 2014). Especially, it has been shown that the ages of intermediate-mass stars tend to disagree with the ages of the T Tauri stars in same clusters (Hartmann 2003).

This system thus seems to confirm the existence of a disagreement between ages derived from low-mass star models and those from intermediate-mass star models. Since the source of uncertainties in the physics and modeling of these two families of objects is different, more efforts and more of those systems are needed to determine whether the remaining uncertainties are inherent to the former or the latter models (or to both)

6.3. Interaction with the circumprimary and circumbinary disks

The orbital elements of the binary system are not in agreement with the orientation and inclination of the outer disk, but they

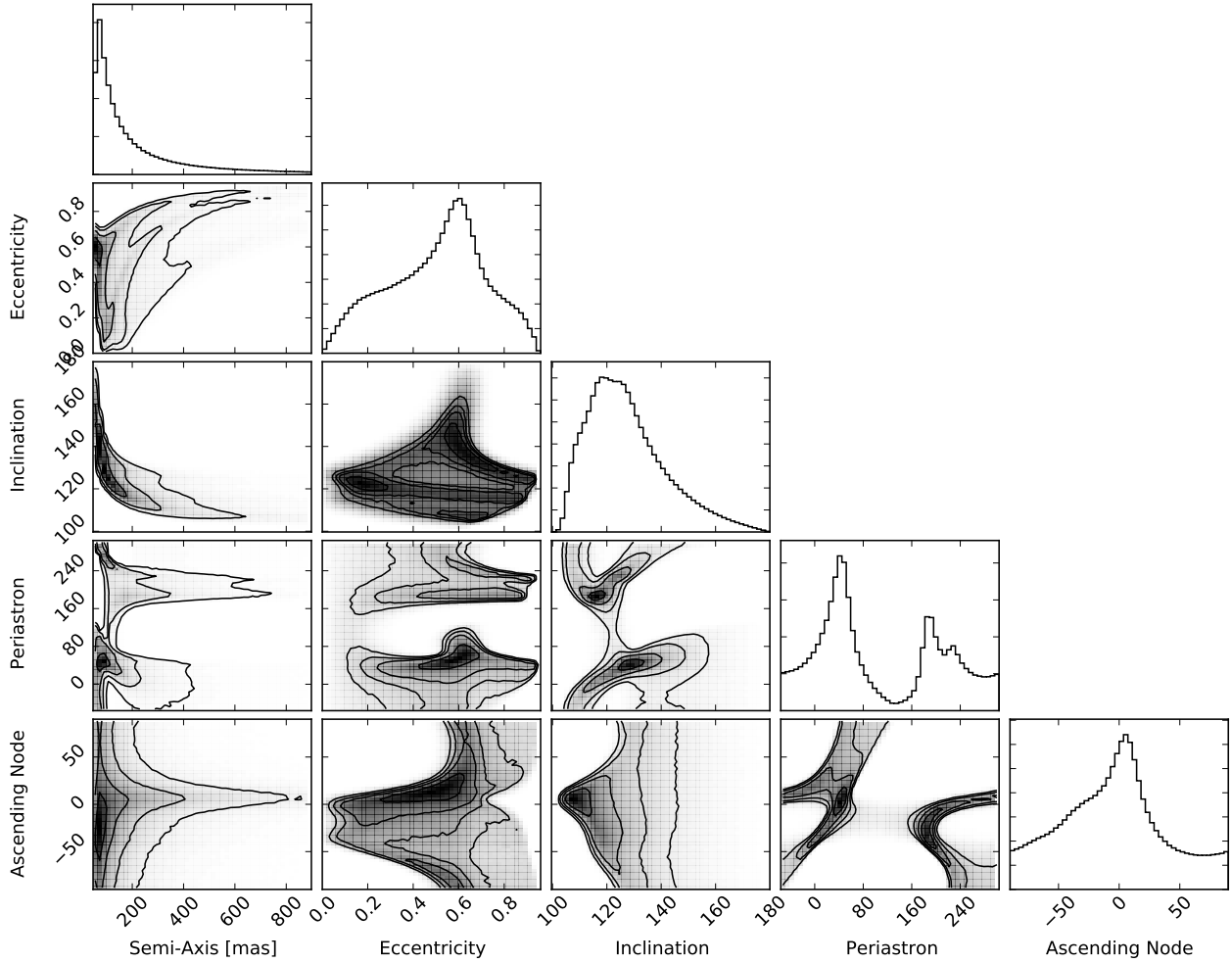


Fig. 7. MCMC simulation for the parameters of the orbit of HD 142527B. We assumed $\mu = 3.2 \times 10^{-5} \text{ arcsec}^3/\text{yr}^2$. All angles are in degrees. Ascending node is calculated for a range of values between -90 and 90 degrees. For comparison, the inner disk as simulated by Casassus et al. (2015a) as a position angle (PA) for the ascending node of -3 degrees, and an inclination with respect to the plane of the sky of 43 degrees (equivalent to 137 degrees following the convention that a clockwise system has an inclination between 90 and 180 degrees).

are in agreement with the parameters of the inner disk derived by Marino et al. (2015) and Casassus et al. (2015a): an inclination of 140 degrees with respect to the sky plane (70 degrees with respect to the outer disk) and a PA of the ascending node at -3 degrees. It is therefore likely that the kinematics of the inner disk are linked to the kinematics of HD 142527B.

The remaining question concerns the gap. Is the inner edge of the outer disk truncated by the companion? If there are orbital solutions that place the companion in the outer disk plane with its apocenter located close to the inner edge of the disk, then the companion may have an ongoing role in sculpting the disk. Figure 8 shows the apocenter distance of the companion versus its inclination to the outer disk plane for all possible orbital solutions. We assumed the outer disk is circular with an inner edge at 90 AU, an inclination of 28 degrees to the sky, and a major axis position angle of 160 degrees (Verhoeff et al. 2011; Perez et al. 2015). The figure shows that for the apocenter distance of the companion to be comparable to the inner edge of the outer disk, its inclination to the outer disk plane must be greater than $\sim 30^\circ$. Furthermore if we assume that the companion lies in the plane of the inner disk (as suggested above) then its apocenter is only around 15 AU, and it is misaligned to the outer disk by $\sim 70^\circ$. Hence the companion cannot simultaneously lie in the outer disk plane and have an apocenter comparable to the inner edge of the

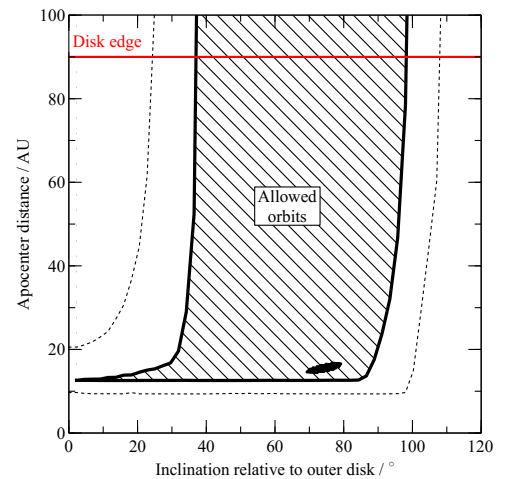


Fig. 8. Possible apocenter distance of the companion vs. its inclination relative to the outer disk plane. The shaded region shows allowed orbits and the dashed lines indicate the 1σ errors on this region. The thick red line is the inner edge of the outer disk, showing that the companion cannot have an apocenter close to this edge and simultaneously orbit in the same plane as the disk. The black area in the lower right of the allowed region shows orbits lying within 5 degrees of the inner disk plane.

outer disk, so it is unlikely that the companion is responsible for truncating the outer disk.

Acknowledgements. S.L. acknowledges fruitful discussions with S. Casassus about the existence of HD 142527B and the inner disk of HD 142527A. This research made use of Astropy, a community-developed core Python package for Astronomy (Astropy Collaboration et al. 2013). This work was supported by the French National Agency for Research (ANR-13-JS05-0005) and the European Research Council (ERC-STG-639248). A.G. and A.S. acknowledge support from NSF Graduate Research Fellowship grant No. DGE-1232825 and NASA grant NNX11AF74G. J.O. acknowledges support from the Millennium Nucleus RC130007 (Chilean Ministry of Economy). I.B. acknowledges the European Research Council through grant ERC-AdG No. 320478-TOFU. Based on observations collected at the European Southern Observatory (ESO) during runs 088.C-0691(A), 090.C-0649(A), 091.C-0572(A), and 094.C-0608(A). Also based on observations obtained at the Gemini Observatory (programs GS-2014A-SV-406 and GS-ENG-GPI-COM), which is operated by the Association of Universities for Research in Astronomy, Inc., under a cooperative agreement with the NSF on behalf of the Gemini partnership: the National Science Foundation (United States), the National Research Council (Canada), CONICYT (Chile), the Australian Research Council (Australia), Ministério da Ciência, Tecnologia e Inovação (Brazil) and Ministerio de Ciencia, Tecnología e Innovación Productiva (Argentina).

References

- Allard, F., Homeier, D., & Freytag, B. 2012, *Phil. Trans. Roy. Soc. London Ser. A*, **370**, 2765
- Astropy Collaboration, Robitaille, T. P., Tollerud, E. J., et al. 2013, *A&A*, **558**, A33
- Avenhaus, H., Quanz, S. P., Schmid, H. M., et al. 2014, *ApJ*, **781**, 87
- Baraffe, I., Chabrier, G., & Gallardo, J. 2009, *ApJ*, **702**, L27
- Baraffe, I., Vorobyov, E., & Chabrier, G. 2012, *ApJ*, **756**, 118
- Baraffe, I., Homeier, D., Allard, F., & Chabrier, G. 2015, *A&A*, **577**, A42
- Billier, B., Lacour, S., Juhász, A., et al. 2012, *ApJ*, **753**, L38
- Cardelli, J. A., Clayton, G. C., & Mathis, J. S. 1989, *ApJ*, **345**, 245
- Casassus, S., van der Plas, G., M., S. P., et al. 2013, *Nature*, **493**, 191
- Casassus, S., Marino, S., Perez, S., et al. 2015a, *ApJ*, **811**, 92
- Casassus, S., Wright, C., Marino, S., et al. 2015b, *ApJ*, **812**, 126
- Castelli, F., & Kurucz, R. L. 2004, *Proc. IAU Symp.*, **210**, A20
- Close, L. M., Follette, K. B., Males, J. R., et al. 2014, *ApJ*, **781**, L30
- D'Antona, F., & Mazzitelli, I. 1997, *Mem. Soc. Astron. It.*, **68**, 807
- de Zeeuw, P. T., Hoogerwerf, R., de Bruijne, J. H. J., Brown, A. G. A., & Blaauw, A. 1999, *AJ*, **117**, 354
- Foreman-Mackey, D., Hogg, D. W., Lang, D., & Goodman, J. 2013, *PASP*, **125**, 306
- Galli, P. A. B., Bertout, C., Teixeira, R., & Ducourant, C. 2013, *A&A*, **558**, A77
- Greenbaum, A. Z., Cheetham, A., Sivaramakrishnan, A., et al. 2014, *SPIE Conf. Ser.*, **9147**, 7
- Hartmann, L. 2003, *ApJ*, **585**, 398
- Kalas, P., Graham, J. R., Fitzgerald, M. P., & Clampin, M. 2013, *ApJ*, **775**, 56
- Knox, K. T. 1976, *J. Opt. Soc. Am.*, **66**, 1236
- Lacour, S., Tuthill, P., Amico, P., et al. 2011, *A&A*, **532**, A72
- Le Bouquin, J.-B. 2014, ArXiv e-prints [arXiv:1408.3227]
- Malfait, K., Bogaert, E., & Waelkens, C. 1998, *A&A*, **331**, 211
- Marino, S., Perez, S., & Casassus, S. 2015, *ApJ*, **798**, L44
- Mendigutía, I., Fairlamb, J., Montesinos, B., et al. 2014, *ApJ*, **790**, 21
- Pearce, T. D., Wyatt, M. C., & Kennedy, G. M. 2015, *MNRAS*, **448**, 3679
- Perez, S., Casassus, S., Ménard, F., et al. 2015, *ApJ*, **798**, 85
- Perrin, M. D., Maire, J., Ingraham, P., et al. 2014, in *SPIE Conf. Ser.*, **9147**, 3
- Preibisch, T., & Mamajek, E. 2008, in *Handbook of Star Forming Regions*, Vol. II (ASP Monograph Publications), 235
- Rodigas, T. J., Follette, K. B., Weinberger, A., Close, L., & Hines, D. C. 2014, *ApJ*, **791**, L37
- Siess, L., Dufour, E., & Forestini, M. 2000, *A&A*, **358**, 593
- Soderblom, D. R., Hillenbrand, L. A., Jeffries, R. D., Mamajek, E. E., & Naylor, T. 2014, *Protostars and Planets VI*, 219
- Thiébaud, E. 2008, in *SPIE Conf. Ser.*, **7013**, 1
- Tuthill, P., Lacour, S., Amico, P., et al. 2010, in *SPIE Conf. Ser.*, **7735**, 1
- van der Marel, N., van Dishoeck, E. F., Bruderer, S., et al. 2013, *Science*, **340**, 1199
- van Leeuwen, F. 2007, *A&A*, **474**, 653
- Verhoeff, A. P., Min, M., Pantin, E., et al. 2011, *A&A*, **528**, A91
- Weingartner, J. C., & Draine, B. T. 2001, *ApJ*, **548**, 296
- Williams, J. P., & Cieza, L. A. 2011, *ARA&A*, **49**, 67
- Wolff, S. G., Perrin, M. D., Maire, J., et al. 2014, in *SPIE Conf. Ser.*, **9147**, 7
- Yi, S., Demarque, P., Kim, Y.-C., et al. 2001, *ApJS*, **136**, 417
- Yi, S. K., Kim, Y.-C., & Demarque, P. 2003, *ApJS*, **144**, 259

¹ LESIA/Observatoire de Paris, PSL, CNRS, UPMC, Université Paris Diderot, 5 place Jules Janssen, 92195 Meudon, France
e-mail: sylvestre.lacour@obspm.fr

² Cavendish Laboratory, University of Cambridge, JJ Thomson Avenue, Cambridge CB3 0HE, UK

³ Institute for Astronomy, University of Edinburgh, Blackford Hill View, Edinburgh EH9 3HJ, UK

⁴ Observatoire de Genève, Université de Genève, 51 chemin des Maillettes, 1290 Versoix, Switzerland

⁵ Johns Hopkins University, Department of Physics and Astronomy, 3400 N. Charles St., Baltimore, MD 21218, USA

⁶ Institute of Astronomy, University of Cambridge, Madingley Road, Cambridge, CB3 0HA, UK

⁷ Sydney Institute for Astronomy, School of Physics, University of Sydney, NSW 2006, Australia

⁸ Space Telescope Science Institute, 3700 San Martin Drive, Baltimore MD 21218, USA

⁹ Astrophysics Group, School of Physics, University of Exeter, Exeter EX4 4QL, UK

¹⁰ European Southern Observatory, Alonso de Cordova 3107, Casilla 19001, Santiago, Chile

¹¹ Univ. Grenoble Alpes, CNRS, IPAG – UMR 5274, 38000 Grenoble, France

¹² École Normale Supérieure, Lyon, CRAL (UMR CNRS 5574), Université de Lyon 1, 69007 Lyon, France

¹³ Max Planck Institut für Astronomie, Königstuhl 17, 69117 Heidelberg, Germany

¹⁴ Instituto de Física y Astronomía, Universidad de Valparaíso, Av. Gran Bretaña 1111, Playa Ancha, Valparaíso, Chile

¹⁵ ICM nucleus on protoplanetary disks, Universidad de Valparaíso, Av. Gran Bretaña 1111, Valparaíso, Chile

¹⁶ School of Physics and Astronomy, University of St Andrews, North Haugh, KY16 6SS, St Andrews, UK

¹⁷ Gemini Observatory, Casilla 603, La Serena, Chile

¹⁸ Gemini Observatory, 670 North A'ohoku Place, Hilo, HI 96720, USA

¹⁹ Durham University, Stockton Road, Durham, DH1 3LE, UK

²⁰ Astronomy Department, University of California, Berkeley CA 94720, USA

²¹ Large Synoptic Survey Telescope, 950N Cherry Av, Tucson AZ 85719, USA

²² Center for Astrophysics and Space Science, University of California San Diego, La Jolla, CA 92093, USA

²³ Kavli Institute for Particle Astrophysics and Cosmology, Stanford University, Stanford, CA 94305, USA

²⁴ Department of Astrophysics, American Museum of Natural History, New York, NY 10024, USA

²⁵ NASA / Armstrong Flight Research Center, 2825 East Avenue P, Palmdale, CA 93550, USA